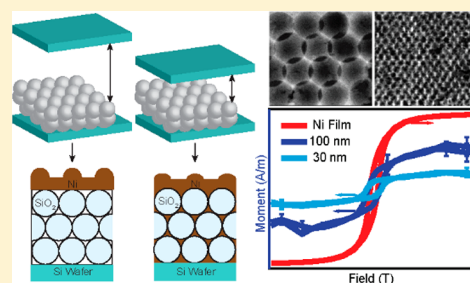


Confined Chemical Fluid Deposition of Ferromagnetic Metalattices

Yunzhi Liu,^{†,⊥} Susan Kempinger,^{‡,⊥} Rongrui He,^{†,⊥} Todd D. Day,^{†,⊥} Parivash Moradifar,^{§,⊥} Shih-Ying Yu,^{§,⊥} Jennifer L. Russell,^{†,⊥} Vincent M. Torres,^{†,⊥} Pengtao Xu,^{†,⊥} Thomas E. Mallouk,^{†,‡,||,⊥} Suzanne E. Mohny,^{§,⊥} Nasim Alem,^{§,⊥} Nitin Samarth,^{‡,⊥} and John V. Badding^{*,†,‡,§,⊥}[†]Department of Chemistry, [‡]Department of Physics, [§]Department of Materials Science and Engineering, ^{||}Department of Biochemistry and Molecular Biology, and [⊥]Materials Research Institute, Penn State University, University Park, Pennsylvania 16802, United States

Supporting Information

ABSTRACT: A magnetic, metallic inverse opal fabricated by infiltration into a silica nanosphere template assembled from spheres with diameters less than 100 nm is an archetypal example of a “metalattice”. In traditional quantum confined structures such as dots, wires, and thin films, the physical dynamics in the free dimensions is typically largely decoupled from the behavior in the confining directions. In a metalattice, the confined and extended degrees of freedom cannot be separated. Modeling predicts that magnetic metalattices should exhibit multiple topologically distinct magnetic phases separated by sharp transitions in their hysteresis curves as their spatial dimensions become comparable to and smaller than the magnetic exchange length, potentially enabling an interesting class of “spin-engineered” magnetic materials. The challenge to synthesizing magnetic inverse opal metalattices from templates assembled from sub-100 nm spheres is in infiltrating the nanoscale, tortuous voids between the nanospheres void-free with a suitable magnetic material. Chemical fluid deposition from supercritical carbon dioxide could be a viable approach to void-free infiltration of magnetic metals in view of the ability of supercritical fluids to penetrate small void spaces. However, we find that conventional chemical fluid deposition of the magnetic late transition metal nickel into sub-100 nm silica sphere templates in conventional macroscale reactors produces a film on top of the template that appears to largely block infiltration. Other deposition approaches also face difficulties in void-free infiltration into such small nanoscale templates or require conducting substrates that may interfere with properties measurements. Here we report that introduction of “spatial confinement” into the chemical fluid reactor allows for fabrication of nearly void-free nickel metalattices by infiltration into templates with sphere sizes from 14 to 100 nm. Magnetic measurements suggest that these nickel metalattices behave as interconnected systems rather than as isolated superparamagnetic systems coupled solely by dipolar interactions.



KEYWORDS: 3D artificial lattices, spin-engineered meta-materials, inverse opals, chemical fluid deposition, ferromagnetic metalattices

Metalattices^{1,2} are artificial three-dimensional (3D) solids³ periodic on a scale of 1–100 nm (Figure 1a). Depending on their detailed structure, they can be notionally subdivided into meta-atoms⁴ (e.g., more capacious regions) linked by metabonds (e.g., thin channels that interconnect meta-atoms). Furthermore, in contrast to superlattices composed of isolated nanocrystals³ coated by, for example, surfactant, metalattices also have an ordered, highly interconnected surface or interface that interweaves their structure. The nanometer-scale, 3D structural order of metalattices can modulate electronic, magnetic, and vibrational degrees of freedom.^{1,2} For example, the size of meta-atoms can be comparable to the typical length scale of the magnetic exchange interaction, or magnetic exchange length, of a ferromagnetic metal such as nickel, which is 47 nm.⁵ Exchange through the metabonds is possible in metalattices whereas weaker dipolar coupling will dominate in arrays of magnetic nanoparticles that are not interconnected. The exchange interaction tends to align neighboring magnetic moments, so features smaller than the

exchange length tend to have uniform, single domain behavior. Modeling suggests the resulting well-ordered magnetic confinement should stabilize a series of unusual magnetic phases, each separated by sharp transitions as the field is increased and with a different topological character (e.g., spirals, “hedgehogs”, streams).² Thus, new physics in “spin-engineered” magnetic metamaterials may be possible if metalattices can be fabricated from ferromagnetic materials, such as nickel, iron, or permalloy.^{2,6}

An archetypal example of a magnetic metalattice is an “inverse opal”⁷ fabricated by infiltration of magnetic metals into the interstitial spaces of a self-assembled close-packed silica spheres with <100 nm diameters (strictly speaking silica spheres this small would not be considered “opals”, but the term inverse opal is commonly used to describe the infiltrated

Received: October 31, 2017

Revised: December 4, 2017

Published: December 13, 2017

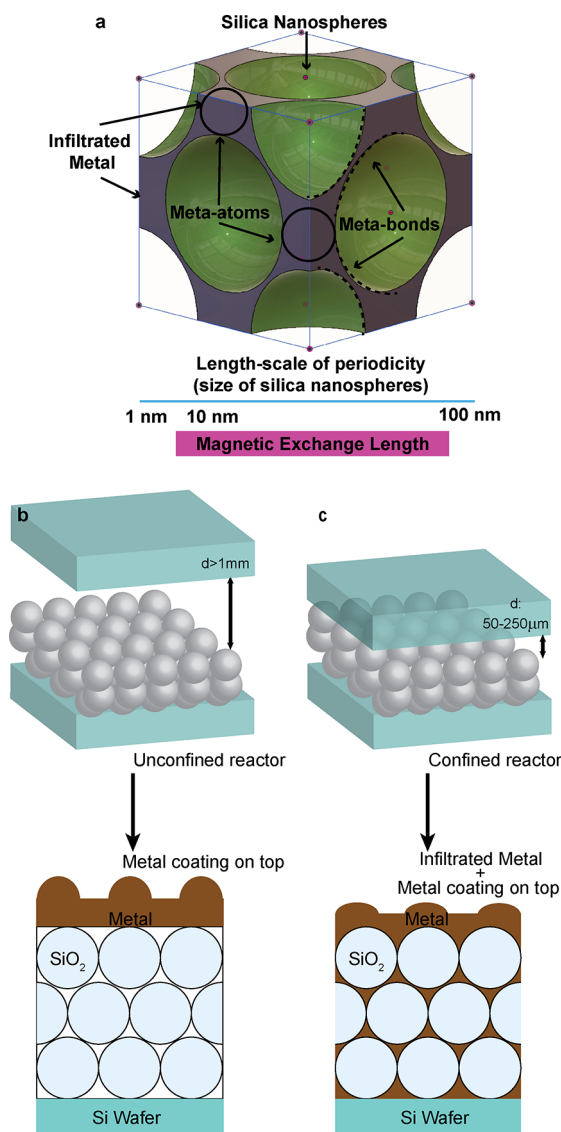


Figure 1. (a) Schematic of an archetypal inverse opal metal metalattice which can be synthesized by infiltration into a self-assembled silica nanosphere template and showing its meta-atoms and metabonds. The ~ 1 – 100 nm length-scale of these inverse opal metallattices differentiates them from conventional inverse opal structures and is commensurate with the range of typical magnetic exchange lengths. (b) “Unconfined” chemical fluid deposition of nickel metal with >1000 μm s or more space above the silica nanosphere template results in a metal coating on top with little infiltration. (c) “Confined” chemical fluid deposition of nickel metal with template with less than 250 μm space above the template allows for infiltration into the sphere template to form a magnetic metalattice with a layer of metal on top.

structures).² These “nanocasted” structures⁸ have an ordered interconnected surface characteristic of a metalattice and meta-atoms formed in the octahedral and tetrahedral template sites with interconnecting metabonds (Figure 1a). Fabrication of metallic inverse opals by methods such as electroplating,^{9,10} electroless deposition,¹¹ metallizing impregnated salt solution,¹² and nanoparticle infiltration¹³ is well developed for silica or polystyrene templates with sphere diameters larger than 100 nm. The resulting materials and related porous ones fabricated by other techniques have been of interest for applications ranging from catalysis to photonics to sensing to energy storage to strong, ultralight materials and more.^{7,14} However, for sphere

diameters less than 100 nm the structures fabricated by these methods largely have limited connectivity throughout the template and instead consist of powders¹⁵ or flakes.¹⁶ Thus, in general nanocasting into templates is a powerful method for synthesis of complex nanostructures,^{8,17} but the range of applicable materials is more limited for templates with sub- 100 nm features (Figure S1) that can be comparable to magnetic exchange lengths, electron and phonon mean free paths, and so forth.^{1,2} The range of applicable materials is especially limited for metals and when void-free or nearly void-free infiltration is required. Electroplating methods moreover require a conducting layer underneath which may interfere with physical properties measurements,^{9,10} such as electrical transport, thermal transport, and magnetic measurements. Controlling precursor diffusion and transport, the balance between heterogeneous and homogeneous nucleation, the rate of growth of the deposit, the exit of reaction byproducts, and avoiding blockage in the very small interstices of sub- 100 nm templates¹⁸ can be a formidable challenge.¹⁹ Moreover, much of the reported work on nanocasting metallic inverse opals has been on noble metals,^{15,16,20} whose precursors are easier to reduce in comparison with more active ferromagnetic metals such as nickel. The sphere size of the template determines the metalattice periodicity.

Conventional chemical vapor deposition is typically not suitable for deposition of interconnected metal inverse opal structures in templates assembled from sub- 100 nm spheres because the mean free path of the precursor molecules at conventional pressures is much larger than the silica template interstices.²¹ Moreover, the vapor pressures of the available precursors for metals such as nickel are generally low, excepting extremely toxic nickel carbonyl ($\text{Ni}(\text{CO})_4$). Transport of high precursor concentrations into small template interstices is therefore difficult. High-pressure chemical fluid deposition (CFD) from organometallic precursors dissolved in supercritical carbon dioxide can transport reactant more rapidly at higher concentrations into nanostructures such as silica nanotemplate voids.^{22,23} The dissolution of precursor into the carbon dioxide allows for higher reactant concentrations while its high diffusivity and relatively low viscosity facilitates transport.²⁴ CFD can conformally coat nanostructures and infiltrate high aspect ratio trenches.²² It can deposit on both insulating and conductive substrates in contrast to electro-deposition methods.^{9,10}

However, we found that at CFD precursor concentrations high enough for deposition of nickel into silica nanotemplates,¹⁸ reaction outside these templates produced films on top of them that precluded infiltration (Figure 1b). Avoiding undesired homogeneous prereaction of precursor before it reaches a surface to heterogeneously deposit is a pervasive challenge in chemical deposition, particularly at the high precursor concentrations desirable for infiltration.²⁵ A counter-current reactor in which reactants enter from opposite sides of the porous sample can help avoid reaction outside it but is not practical for templates supported on impermeable silicon wafers,¹⁹ such as we use in the present study. Instead, we chose to use a confined reactor in which no space has any linear dimension larger than a chosen value (Figures 1c and S2) on the order of tens to hundreds of micrometers. Deposition experiments with silane precursor to deposit silicon films in a silica capillary reveal that appropriate confinement that increases the surface-area-to-volume ratio can also increase the surface reaction rate relative to the bulk reaction rate

throughout the reactor.²⁶ The change in the balance of reaction rates can suppress homogeneous formation of particles and flakes²⁵ that can collect on a template surface to block infiltration. Here we report the synthesis of nickel metalattice films using supercritical fluid deposition in a spatially confined reactor at a relatively low temperature of 100 °C for nickel (Figures S2–S4). The films are of macroscopic dimensions, square millimeters in area, and 200–1500 nm thick. Their magnetic properties are suggestive of confined magnetic meta-atoms interacting through linking metabonds in a ferromagnetic metalattice.

Hunde and Watkins reported chemical fluid deposition of Ni on planar substrates and into high aspect ratio trenches.^{22,27} They used bis(cyclopentadienyl) nickel(II) (nickelocene) precursor and hydrogen gas as a reducing agent. The substrate temperatures were 175 to 200 °C while reactor pressures were 190–230 bar.²⁷ At lower temperatures, predeposition of catalytic metal particles or films on insulating substrates was required to initiate the reduction of the precursor.²² It is desirable to simplify the deposition process and avoid the extra step of predeposition.²⁷ Later, Peng et al. reported that longer reaction times of 7–8 h with hydrogen allowed for reduction of precursor at 70 °C at 35 MPa without the need for catalytic particles or films.²⁸ We attempted to infiltrate self-assembled 30 nm (and also 100 nm) silica sphere templates (Figure S1) using similar chemistry at 100 °C and 40 MPa with a reaction time of 5 h in an unconfined reactor (Figure 1b). Most of the precursor reacted outside the template, forming an exterior nickel film that appeared to block further infiltration (Figure 2a,b). To attempt to avoid formation of this exterior film, which was hypothesized to arise because of too rapid homogeneous reaction, we deposited nickel with a 50 μm confining space above the template (Figure 1c), otherwise under the same conditions. The nickel now infiltrated the substrate, but only partially, forming interconnected metal networks with large spaces between them (Figure 2c,d). Evidently the transport of reactant is insufficient with so much confinement. Then we increased the thickness of the spatially confined region to 250 μm and near complete, interconnected metal networks formed (Figure 2e,f). Cross-sectional bright-field and high-angle annular dark-field (HAADF) transmission electron microscopy (TEM) images, and energy dispersive X-ray spectroscopy (EDS) mapping (Figure 2e,f) suggest the nickel fills at least 95% of the template interstices. In contrast, with 50 μm confinement the filling is unsatisfactory, only 40% (Figure 2d). It appears that with either 50 or 250 μm confinement, the reaction rate at high pressure is too high to avoid deposition of a layer of nickel on top of the metalattice, which we later remove for magnetic property measurements.

Having optimized the high-pressure deposition chemistry and the reactor spatial confinement for 30 nm sphere templates, we infiltrated nickel into 100 nm sphere templates (Figure 3a–e) and 14 and 70 nm templates¹⁸ (Figure S5) to investigate the impact of metalattice periodicity and magnetic confinement on properties. Back scattered scanning electron microscopy (SEM), which probes deeply into a material, reveals a well-ordered 100 nm nickel metalattice (Figure 3a). The nickel metalattices are millimeters in length and width with thickness ranging from 200 to 1500 nm. Secondary electron SEM imaging (Figure 3b), HAADF TEM and Ni EDS mapping (Figure 3c–e) reveal good order without many voids.

Selected-area electron diffraction shows that both 30 and 100 nm metalattices are composed of face-centered-cubic (fcc)

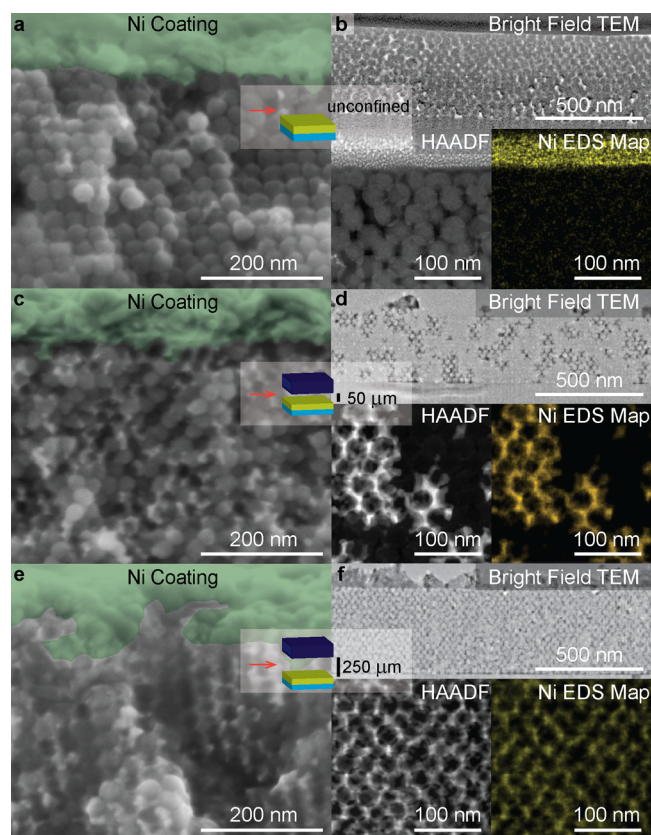


Figure 2. (a) SEM cross-sectional image of sample after unconfined chemical fluid deposition into 30 nm silica nanosphere template with a macroscopic space >1 mm high above the film. A nickel film forms on top of the template and there is little infiltration as evidenced by the similarity of the image to that of an empty template such as in Figure S1b and its difference from subsequent infiltrated images. (b) Bright-field and HAADF TEM show most of the interstitial space between the silica spheres is not infiltrated; perhaps most definitively, Ni EDS mapping, shows no evidence for infiltration. (c) SEM cross-sectional image of confined chemical fluid deposition into 30 nm silica sphere template with 50 μm of spatial confinement. The infiltration observed in bright-field and HAADF TEM and Ni EDS chemical mapping (d) is only partial. The tearing of the nickel upon cross sectioning makes interpretation of the SEM images (c) more difficult, but more infiltration is evident. (e) SEM cross-sectional image of chemical fluid deposition into 30 nm silica sphere template with 250 μm of spatial confinement. A better developed metalattice is evident in this SEM cross section, as well as in bright-field and HAADF TEM and Ni EDS mapping (f).

polycrystalline nickel (Figure S6). We investigated the chemical composition of the as-deposited 30 nm Ni metalattices by X-ray photoelectron spectroscopy (XPS), collecting both depth profiles and survey spectra (Figure S7). Metals deposited from organometallic precursors may have carbon impurities, especially if tortuous, nanoscale voids in templates such as nanoscale silica spheres or the spatial confinement employed for nickel metalattice synthesis constricts the exit of both the H_2 reductant and the organic reaction byproducts. Carbon and oxygen in the top Ni layer were at or near the background level for the XPS instrument, 2.2% and 1.2%, respectively. In the metalattice, the carbon content was 3.6%, slightly above background. However, the roughness of the metalattice may impact the accuracy of this measurement such that it is comparable to the background. It is likely that the carbon

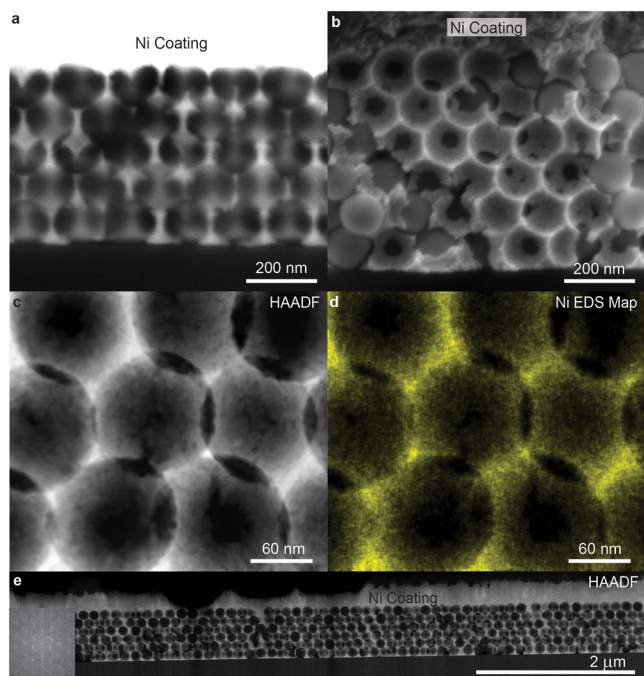


Figure 3. (a) Backscattered SEM cross-sectional image of a 100 nm sphere Ni metalattice, showing a 3D Ni network. (b) Secondary SEM cross-sectional image of 100 nm Ni metalattice at a different location from (a). Some tearing of the metalattice upon cross sectioning is observed. (c) High-magnification HAADF TEM image of a 100 nm Ni metalattice. (d) Cross-sectional image of TEM EDS Ni chemical map of a 100 nm Ni metalattice. (e) Low-magnification HAADF image of a 100 nm Ni metalattice (inset: FFT of the image, confirming long-range order).

content is 3.6% or less. Thus, the nickel metalattices have at most only small amounts of carbon contamination. To realize this lower level of carbon impurity it was important to deposit at a relatively low temperature (100 °C) and with a high pressure of hydrogen (40 MPa). At a higher reaction temperature of 175 °C under otherwise identical reaction conditions isolated Ni nanoparticles were deposited that were dispersed around the silica spheres, with a much lower Ni filling fraction and much more carbon contamination (Figure S8). There is no evidence of any second phase in the selected area diffraction patterns.

The magnetic properties of nickel inverse opal metalattices, which have periodicities of 100 nm or less and associated meta-atoms with diameters less than 50 nm, should differ from those of larger nickel inverse opals as the magnetic confinement increases. Previous studies have shown that the coercive field required to reverse the magnetization of a nickel inverse opal depends strongly on both its periodicity¹⁰ and the film thickness.²⁹ Nickel inverse opals with periodicities longer than 100 nm have octahedral sites about the same size as or larger than the exchange length and can support complex magnetic structures such as curling domain modes for which

the magnetization tends to form closed loops.² They also support more spatial variation in neck magnetization, so the octahedral and tetrahedral sites are predominantly coupled by longer range dipolar interactions between adjacent sites.² These interactions can couple isolated nanoparticles as well as interconnected tetrahedral and octahedral sites in inverse opals, forming a system that seeks to minimize its magneto-static energy. As the inverse opal periodicity decreases to that of metalattices, around 100 nm, the magnetic structures become too small to support curling domain modes. The coercive field should decrease with decreasing sphere size, the nanostructures should behave as single domain elements, and the dominant coupling mechanism should become exchange mediated through the metabonds.^{2,10,30} Metabond mediated exchange is a defining characteristic of a magnetic metalattice that allows for the diversity of topologically distinct structures.

We investigated the magnetic properties of the 100 and 30 nm metalattices by superconducting quantum interference device (SQUID) magnetometry, after removing the top Ni layer using hydrochloric acid (HCl) spin-etching. We applied magnetic fields along the film plane of the sample (an in-plane orientation). The silica sphere templates that define the nickel metalattices could in principle have fcc (*abc* stacking), hexagonal close-packed (hcp) (*ab* stacking) or other stacking patterns. However, we found that 30 nm nonmetallic metalattices were fcc by an analysis of TEM images at different angles (unpublished). Although we did not check the structure of the nickel metalattices, they are likely also fcc as the templates were synthesized under identical conditions. For any of the close-packed structures, the electron microscopy images reveal that the sphere layers are largely parallel to the substrate, as would be expected. For fcc metalattices the [111] metalattice crystal direction will be normal to the substrate plane. While synthesis of single crystal silica sphere templates may be possible, thus far it is reasonable to expect some variation in the orientation of different domains in films millimeters across such that the domain orientation rotates around [111].

As one of the interesting properties of magnetic metalattice systems is the potential for abrupt topological transitions,² we measured field sweeps at low temperature to minimize thermal effects (3 K). For magnetic field sweeps, we removed the diamagnetic background as approximated by a linear fit to the raw data at high field. We also studied the magnetization as a function of temperature from 3 to 305 K. Modeling suggests that the easy axis of magnetization of fcc permalloy metalattices (neglecting crystalline anisotropy and magnetostriction) lies in the [001] direction, which is 54.7° from [111] and thus not in the plane.² Topological transitions are predicted to occur along the easy axis as well as in other directions.

We first consider the characteristics of the hysteresis in our samples (Table 1). Thirty nanometers and 100 nm metalattices consist of 6.8 and 22.5 nm tetrahedral and 12.4 and 41.4 nm octahedral meta-atoms, respectively. The meta-atoms are interconnected by metabonds as small as 2.3 nm in 30 nm metalattices and 7.8 nm in 100 nm ones. Previous studies on

Table 1. Magnetic Hysteresis Characteristics of Ni Film and Metalattice Samples at 3 K

Ni Sample	thickness (nm)	H_C (T)	M_R (A/m)	M_S (A/m)	squareness	$M_s/M_{s, \text{Film}}$
film	230	0.018	0.0112	0.038	0.29	1
100 nm	600	0.029	0.000070	0.00035	0.20	0.00921
30 nm	1500	0.035	0.000037	0.00011	0.34	0.00289

inverse opal Ni structures show these sizes lie in the single domain regime.¹⁰ This was deduced from the dependence of the coercive field (H_C) as a function of the periodicity of the inverse opal: As predicted by theory,² H_C reaches a maximum value when the length scale of the system becomes too small to support curling domain modes.³¹ Below this transition, H_C decreases as the length scales decrease, in qualitative agreement with the behavior of single domain Ni nanoparticles.³² Film thickness also strongly influences H_C for magnetic inverse opal structures.^{10,29} As our films are different thicknesses, we cannot directly observe a trend in coercivity. However, the coercivity for both metalattice samples shows a significant enhancement over the coercivity of the continuous Ni film (Figure 4a)

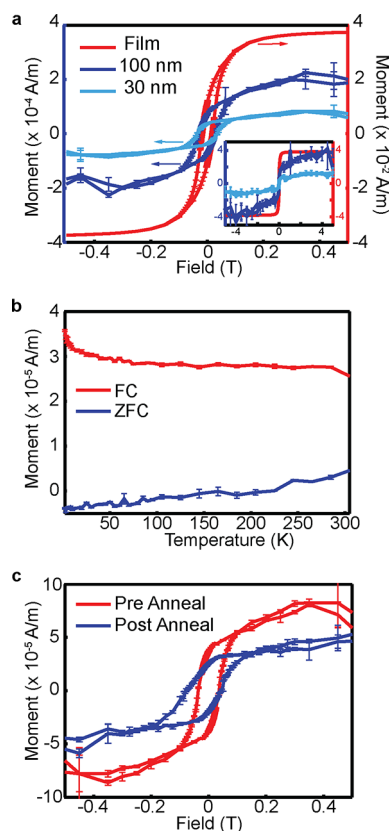


Figure 4. (a) Field sweeps of as-deposited 30 and 100 nm Ni metalattices, and Ni bulk film (inset: hysteresis loops from -5 to 5 T). (b) Temperature sweeps, FC and ZFC show no superparamagnetic blocking behavior. (c) Field sweeps of 30 nm Ni metalattices before and after annealing in flowing nitrogen. The loop for the annealed sample shifts to the left. Field sweeps were taken at 3K.

because domain walls cannot easily move through their structure. The saturation field (H_S) at which the saturation magnetization is reached for the metalattice also is much larger than that of the bulk film. Comparison of the field sweeps on Ni metalattices and their corresponding silica nanosphere templates confirms that the dominant magnetic signal for metalattices come from the infiltrated Ni, rather than the templates (Figure S9).

Additionally, we observe an increase in squareness (defined as the ratio of the remnant magnetization (M_R) to the saturation magnetization (M_S)) as the size is decreased from 100 to 30 nm, in agreement with observations of larger inverse opals.^{10,31} For the 30 nm metalattices, the thin necks give a

strong constraint on the magnetization direction, and we expect a one-step transition with no intermediate states. As the metabonds increase in size, their magnetic moments soften and allow for more spatial variation in magnetization.² These more complex domain patterns allow for intermediate states thus resulting in a decrease in squareness. Theoretical models predict an intermediate state in the 100 nm metalattices, in which adjacent layers of the metalattices are antiferromagnetically coupled, which we do not observe. The neglect of the magnetocrystalline anisotropy of Ni in these models could change the lattice constant required for the onset of intermediate states. Also, the Ni metalattice consists of multiple crystal domains formed from template sphere packings. A lower bound of tens of microns on the size of these domains is evident from SEM images of their top surfaces (at longer length scales associated with lower magnifications it becomes difficult to resolve individual spheres). The different orientations of these domains might smooth out sharp features in the hysteresis. Further increase in the size of the metalattices allows for the onset of significant curling in the octahedral sites, which leads to additional topological transitions and the development of discrete jumps in the magnetization during the reversal process.² The 30 nm sphere sizes are too small to expect this behavior. The metalattice Ni is polycrystalline, but studies on single crystal nanowires suggest that single crystal Ni could show further enhanced coercivity and squareness.³³ High-resolution TEM (HRTEM) reveals that the polycrystalline Ni grains have sizes on the order of 5 to 10 nm (Figure S10), smaller than the magnetic exchange length. Grains this small are in the random anisotropy regime, in which the magnetic anisotropy should be reduced as the exchange coupling averages it out over several grains.³⁴ As the modeling predictions of a series of topological phases did not account for anisotropy,² reduction of it might make the actual magnetic behavior follow them more closely.

Because the Ni metalattices are in the single domain size regime, we expect that magnetic domain walls will be confined to the necks and that the meta-atoms will behave as single domain particles. Disconnected single domain Ni nanoparticles and superlattices coupled by dipolar interactions show hysteresis at low temperatures.^{32,35} However, as the thermal energy is increased, thermal fluctuations rather than applied fields dominate the magnetization direction of the particles. Above this transition temperature (T_B), the particles are said to be “unblocked” and display superparamagnetic behavior.³⁶ T_B is observed as the temperature at which field-cooled (FC) and zero-field-cooled (ZFC) temperature sweeps converge, accompanied by a peak in the ZFC scan, and is below room temperature for nanoparticles in our size ranges.^{32,35} Granular Ni nanotubes and larger cobalt (Co) inverse opals consisting of agglomerated particles also display superparamagnetism.^{37,38} However, for metalattices we observe no such blocking transition (Figure 4b). The absence of this transition is evidence for the neck-mediated exchange coupling expected in this system and that the metalattices are behaving as a truly interconnected system. Nickel exhibits itinerant magnetism, so the presence of grain boundaries within the metalattices should not have a major impact on the exchange as long as there are no gaps or significant oxide in them (polycrystalline Ni behaves as a ferromagnet, for example). Oxide would not be expected to form under the reducing conditions used for deposition and oxygen is excluded from the reactants as well. The observed magnetic behavior supports this hypothesis because it is

consistent with a well-interconnected nanoscale geometry, free from gaps or oxide that could divide the metalattices into isolated particles.

Finally, nanoscale samples often show a decrease in saturation magnetization with increasing surface-area-to-volume ratio, attributed to magnetic dead layers at surfaces, oxidation layers, or changes in cohesive energy.^{32,33} We also observe a strong decrease in the magnetic signal at 5 T from the metalattices relative to the bulk film. The decrease is stronger than usually observed for nanoparticles. Metalattices have a very high surface-area-to-volume ratio, so it is reasonable for surface effects to be very important. Alternatively, the system might be incompletely saturated at 5 T and instead be in a stable intermediate state due to strong domain pinning, where domain walls become “stuck” in local energy minima because of the complicated metalattice geometry. We also cannot rule out the presence of higher field dynamics. This question could potentially be more thoroughly addressed using small angle neutron scattering or higher field studies.

After the Ni metalattices are annealed in flowing nitrogen with the silica spheres remaining inside them, electron diffraction and EDS mapping reveal the formation of an antiferromagnetic NiO surface (Figure S11). Furthermore, the center of the hysteresis loops shifts to the left from zero, indicative of an exchange bias effect (Figure 4c).³⁹ This exchange bias effect between ferromagnetic nickel and antiferromagnetic nickel oxide has also been observed in Ni core/NiO shell nanoparticles,⁴⁰ as well as in Co inverse opals with grains that are coated with cobalt oxide.³⁸ The absence of an exchange bias effect in all as-grown metalattices which have hysteresis loops centered at zero suggests that no significant surface oxidation occurs during the deposition process. It is possible to etch out the silica spheres (Supporting Information and Figure S12), which allows for a nanoporous metalattice that could be chemically functionalized or otherwise modified to control magnetic, thermal, or electronic properties or make new metalattices. Thus, it seems likely that the 3D ordered nanostructured metalattices can be modified while largely keeping their structure and order intact. In contrast, nanoparticles chemically modified in solution phase generally are assembled after functionalization. Confined high-pressure deposition of silicon²⁶ within a transition metal metalattice, for example, followed by annealing to induce solid state reaction could allow for magnetic transition metal silicide metalattices. The 3D ordered nanostructured metalattices of a diversity of materials could then be realized, especially considering the variety of templates of different symmetries (e.g., binary sphere templates, gyroid mesoporous silica, etc.) that could be infiltrated.

■ ASSOCIATED CONTENT

■ Supporting Information

The Supporting Information is available free of charge on the ACS Publications website at DOI: [10.1021/acs.nanolett.7b04633](https://doi.org/10.1021/acs.nanolett.7b04633).

Experimental description of metalattice synthesis and characterization, the deposition apparatus and a reactor illustration, higher-temperature metallization experiments, SEM of empty templates and Ni metalattices of additional sizes, further chemical analysis, SQUID magnetometry raw field sweep data, and TEM images of annealed Ni metalattices (PDF)

■ AUTHOR INFORMATION

Corresponding Author

*E-mail: jbadding@chem.psu.edu.

ORCID

Pengtao Xu: 0000-0002-4470-446X

John V. Badding: 0000-0002-4517-830X

Author Contributions

Y.L. synthesized the nickel metalattices with assistance from V.M.T. from templates assembled by J.L.R. P.X. assisted with wet etch processing under the guidance of T.E.M. S.K. collected and interpreted magnetic measurements with guidance from N.S. Y.L., T.D.D., and R.H. developed confined chemical vapor deposition. P.M., S.-Y.Y., N.A., and S.E.M. collected and analyzed TEM data. J.V.B., N.S., S.K., and Y.L. conceived and planned the experiments. Y.L., J.V.B., N.S., and S.K. wrote the manuscript, which was discussed, reviewed, and approved by all authors.

Notes

The authors declare no competing financial interest.

■ ACKNOWLEDGMENTS

We thank V. H. Crespi for valuable discussions and acknowledge the Penn State Materials Characterization Lab and Nanofabrication Lab for characterization and process support. This work was supported by the Penn State Center for Nanoscale Science, an NSF-sponsored Materials Science and Engineering Center under award DMR-1420620.

■ REFERENCES

- (1) Han, J. E.; Crespi, V. H. *Phys. Rev. Lett.* **2001**, *86*, 696–699.
- (2) Han, J. E.; Crespi, V. H. *Phys. Rev. Lett.* **2002**, *89*, 197203.
- (3) Murray, C. B.; Kagan, C. R.; Bawendi, M. G. *Annu. Rev. Mater. Sci.* **2000**, *30*, 545–610.
- (4) Collier, C. P.; Vossmeier, T.; Heath, J. R. *Annu. Rev. Phys. Chem.* **1998**, *49*, 371–404.
- (5) O’Handley, R. C. *Modern Magnetic Materials*. Wiley: New York, 2000; pp 296.
- (6) Wang, R. F.; Nisoli, C.; Freitas, R. S.; Li, J.; McConville, W.; Cooley, B. J.; Lund, M. S.; Samarth, N.; Leighton, C.; Crespi, V. H.; Schiffer, P. *Nature* **2006**, *439*, 303–306.
- (7) Hu, J.; Stein, A. *Macroporous Materials Synthesized by Colloidal Crystal Templating*. In *Handbook of Solid State Chemistry*; Dronskowski, R., Kikkawa, S., Stein, A., Eds.; Wiley: Weinheim, 2017; Vol. 4, pp 243–274.
- (8) Lu, A.-H.; Zhao, D.; Wan, Y. *Nanocasting: A Versatile Strategy for Creating Nanostructured Porous Materials*. RSC Publishing: Cambridge, UK, 2010.
- (9) Barako, M. T.; Sood, A.; Zhang, C.; Wang, J.; Kodama, T.; Ashghhi, M.; Zheng, X.; Braun, P. V.; Goodson, K. E. *Nano Lett.* **2016**, *16*, 2754–2761.
- (10) Hao, Y.; Zhu, F.; Chien, C.; Searson, P. C. *J. Electrochem. Soc.* **2007**, *154*, D65–D69.
- (11) Jiang, P.; Cizeron, J.; Bertone, J. F.; Colvin, V. L. *J. Am. Chem. Soc.* **1999**, *121*, 7957–7958.
- (12) Yan, H.; Blanford, C. F.; Holland, B. T.; Parent, M.; Smyrl, W. H.; Stein, A. *Adv. Mater.* **1999**, *11*, 1003–1006.
- (13) Velev, O. D.; Kaler, E. W. *Adv. Mater.* **2000**, *12*, 531–534.
- (14) Schaedler, T. A.; Jacobsen, A. J.; Torrents, A.; Sorensen, A. E.; Lian, J.; Greer, J. R.; Valdevit, L.; Carter, W. B. *Science* **2011**, *334*, 962–965.
- (15) Egan, G. L.; Yu, J.-S.; Kim, C. H.; Lee, S. J.; Schaak, R. E.; Mallouk, T. E. *Adv. Mater.* **2000**, *12*, 1040–1042.
- (16) Ye, L.; Wang, Y.; Chen, X.; Yue, B.; Tsang, S. C.; He, H. *Chem. Commun.* **2011**, *47*, 7389–7391.
- (17) Baumberg, J. J. *Nat. Mater.* **2006**, *5*, 2–5.

- (18) Russell, J. L.; Noel, G. H.; Warren, J. M.; Tran, N. L. L.; Mallouk, T. E. *Langmuir* **2017**, *33*, 10366–10373.
- (19) Gummalla, M.; Tsapatsis, M.; Watkins, J. J.; Vlachos, D. G. *Ind. Eng. Chem. Res.* **2003**, *42*, 1321–1328.
- (20) Li, C.; Dag, Ö.; Dao, T. D.; Nagao, T.; Sakamoto, Y.; Kimura, T.; Terasaki, O.; Yamauchi, Y. *Nat. Commun.* **2015**, *6*, 6608.
- (21) Sparks, J. R.; Sazio, P. J.; Gopalan, V.; Badding, J. V. *Annu. Rev. Mater. Res.* **2013**, *43*, 527–557.
- (22) Blackburn, J. M.; Long, D. P.; Cabañas, A.; Watkins, J. J. *Science* **2001**, *294*, 141–145.
- (23) Watkins, J. J.; Blackburn, J. M.; McCarthy, T. J. *Chem. Mater.* **1999**, *11*, 213–215.
- (24) Romang, A. H.; Watkins, J. J. *Chem. Rev.* **2010**, *110*, 459–478.
- (25) Jones, A. C.; Hitchman, M. L. *Chemical Vapour Deposition: Precursors, Processes and Applications*. Royal Society of Chemistry: Cambridge, UK, 2009.
- (26) Baril, N. F.; He, R. R.; Day, T. D.; Sparks, J. R.; Keshavarzi, B.; Krishnamurthi, M.; Borhan, A.; Gopalan, V.; Peacock, A. C.; Healy, N.; Sazio, P. J. A.; Badding, J. V. *J. Am. Chem. Soc.* **2012**, *134*, 19–22.
- (27) Hunde, E. T.; Watkins, J. J. *Chem. Mater.* **2004**, *16*, 498–503.
- (28) Peng, Q.; Spagnola, J. C.; Parsons, G. N. *J. Electrochem. Soc.* **2008**, *155*, D580–D582.
- (29) Zhukov, A.; Goncharov, A.; De Groot, P.; Ghanem, M.; Bartlett, P.; Boardman, R.; Fangohr, H.; Novosad, V.; Karapetrov, G. *Appl. Phys. Lett.* **2006**, *88*, 062511.
- (30) Zeng, H.; Li, J.; Liu, J. P.; Wang, Z. L.; Sun, S. H. *Nature* **2002**, *420*, 395–398.
- (31) Nielsch, K.; Wehrspohn, R.; Barthel, J.; Kirschner, J.; Gösele, U.; Fischer, S.; Kronmüller, H. *Appl. Phys. Lett.* **2001**, *79*, 1360–1362.
- (32) Murray, C.; Sun, S.; Doyle, H.; Betley, T. *MRS Bull.* **2001**, *26*, 985–991.
- (33) Pan, H.; Liu, B.; Yi, J.; Poh, C.; Lim, S.; Ding, J.; Feng, Y.; Huan, C.; Lin, J. *J. Phys. Chem. B* **2005**, *109*, 3094–3098.
- (34) Löffler, J. F.; Meier, J. P.; Doudin, B.; Ansermet, J. P.; Wagner, W. *Phys. Rev. B: Condens. Matter Mater. Phys.* **1998**, *57*, 2915–2924.
- (35) Ely, T. O.; Amiens, C.; Chaudret, B.; Snoeck, E.; Verelst, M.; Respaud, M.; Broto, J.-M. *Chem. Mater.* **1999**, *11*, 526–529.
- (36) Chen, Q.; Zhang, Z. J. *Appl. Phys. Lett.* **1998**, *73*, 3156–3158.
- (37) Pereira, A.; Palma, J. L.; Denardin, J. C.; Escrig, J. *Nanotechnology* **2016**, *27*, 345709.
- (38) Krivorotov, I. N.; Yan, H. W.; Dahlberg, E. D.; Stein, A. J. *Magn. Mater.* **2001**, *226–230*, 1800–1802.
- (39) Nogués, J.; Schuller, I. K. J. *Magn. Mater.* **1999**, *192*, 203–232.
- (40) Johnston-Peck, A. C.; Wang, J.; Tracy, J. B. *ACS Nano* **2009**, *3*, 1077–1084.